Aerodynamic Optimization of Micro Aerial Vehicle

S. P. Yeong[1†] and S. S. Dol[2]

[1] *Mechanical Engineering Department, Curtin University, Miri, Sarawak, 98009, Malaysia*
[2] *Petroleum Engineering Department, Curtin University, Miri, Sarawak, 98009, Malaysia*

†*Corresponding Author Email: yeong.siew.ping@postgrad.curtin.edu.my*

ABSTRACT

Computational fluid dynamics (CFD) study was done on the propeller design of a micro aerial vehicle (quadrotor-typed) to optimize its aerodynamic performance via Shear Stress Transport K-Omega (SST k-ω) turbulence model. The quadrotor model used was WL-V303 Seeker. The design process started with airfoils selection and followed by the evaluation of drone model in hovering and cruising conditions. To sustain a 400g payload, by Momentum Theory an ideal thrust of 5.4 N should be generated by each rotor of the quadrotor and this resulted in an induced velocity of 7.4 m/s on the propeller during hovering phase, equivalent to Reynolds number of 10403 at 75% of the propeller blade radius. There were 6 propellers investigated at this Reynolds number. Sokolov airfoil which produced the largest lift-to-drag ratio was selected for full drone installation to be compared with the original model (benchmark). The CFD results showed that the Sokolov propeller generated 0.76 N of thrust more than the benchmark propeller at 7750 rpm. Despite generating higher thrust, higher drag was also experienced by the drone installed with Sokolov propellers. This resulted in lower lift-to-drag ratio than the benchmark propellers. It was also discovered that the aerodynamic performance of the drone could be further improved by changing the rotating direction of each rotor. Without making changes on the structural design, the drone performance increased by 39.58% in terms of lift-to-drag ratio by using this method.

Keywords: Aerodynamics; Airfoil; CFD; Lift-to-drag ratio; Quadrotor; Sokolov.

NOMENCLATURE

A	propeller disc area	R	blade radius
AOA	angle of attack	S	drone frontal area
c	chord length	T_C	cruising thrust
C_P	pressure coefficient	T_H	hovering thrust
D_S	streamwise drag of the drone	UVP	ultrasound Velocity Profiler
D_V	vertical drag of the drone	ρ	air density
MAV	micro aerial vehicle	μ	kinematic viscosity

1. INTRODUCTION

This project was carried out to optimize the aerodynamic performance of a micro aerial vehicle (MAV). The design process of the propeller was completed through computational fluid dynamics (CFD) simulations and the influences of each design parameters on the quadrotor were evaluated. Three CFD models were set up to simulate the propeller and aircraft performance in two flight conditions: hovering and cruising. The aerodynamic properties of the modified design were compared with the original design (benchmark) and discussed.

The MAV model studied in this project is WL-

V303 Seeker Quadcopter manufactured by WL Toys. A picture of the actual model is shown in Fig. 1.

In this project, the MAV propeller design was modified such that it could generate the required thrust to carry a payload of 400g through improved aerodynamic properties. This would help to reduce the power consumption of motors due to extra loading. The payload could either be a camera system for surveillance activity or other light weight items such as energy bars and drinking water in search and rescue operation (SAR).

There have been very few studies about the aerodynamic performance of a quadrotor based on

mechanical design aspect as focus are mostly on the control behaviour of quadrotor via its electronic system (Naidoo, Stopforth and Bright 2011; Yeong, King and Dol 2015). For this project, different airfoils were initially studied to compare their performances at low Reynolds number. The original 9×4.5inch propeller of the drone (as shown in Fig. 2) will serve as a benchmark for the new propeller design investigation.
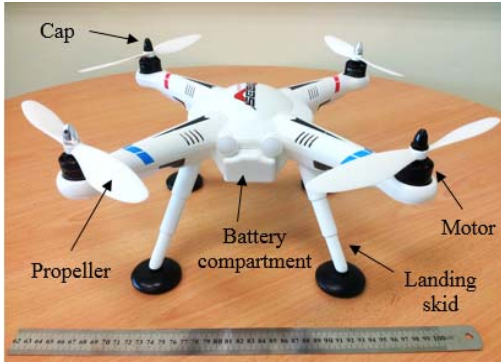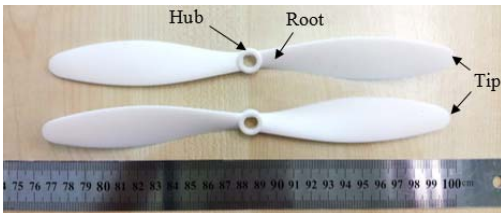

Fig. 1. WL-V303 Seeker model.

Fig. 2. Benchmark Propellers (Top: Rotate ACW, Bottom: Rotate CW).

2. THEORIES

The lift and drag coefficient for a propeller can be determined as

$$C_L = LF \Big/ \frac{1}{2}\rho V^2 S \tag{1}$$

$$C_D = DF \Big/ \frac{1}{2}\rho V^2 S \tag{2}$$

where S is the propeller planform area (m²), LF is the lift force (N), DF is the drag force (N), ρ is the air density (=1.18415kg/m³) and V is the velocity of the propeller (m/s). Kutta-Joukowski circulation theorem states that the airfoil's lift LF can be related to circulation as:

$$LF = -\rho V \Gamma \tag{3}$$

where Γ is defined by the integral around a close curve C in the fluid flow field enclosing the airfoil (Hardi and Schlichenmaier 2005). Circulation Γ is assumed negative in CW direction (Dol, Kopp and Martinuzzi 2008).

To study the aerodynamic characteristics of the airfoil, the velocity experienced by the propeller needs to be pre-determined as it affects the amount

of thrust generated. Theoretical velocity for hovering case was calculated using the Momentum theory. The theory assumed the fluid flow to be inviscid and incompressible (Gudmundsson 2014). The fluid pressure and density at far field upstream and downstream are constant. Flowing through a rotating propeller that is assumed to be an actuator disc with negligible thickness which has no viscous effect, the flow was accelerated to have a higher velocity downstream. The mass flow rate through the disc is given as $\dot{m} = \rho A v_h$ where A is the propeller disc area and v_h is the induced velocity by the propeller disc (m/s). The thrust acting on the disc due to change of momentum is therefore (Yahya 2010)

$$T = \dot{m}(c_s - c_u) = \rho A v_h (c_s - c_u) \tag{4}$$

where c_s is the upstream velocity (m/s) and c_u is the downstream velocity (m/s). For hovering case, $c_s = 0$ and $c_u = v_h$, Rearrange,

$$v_h = \sqrt{T_H /(2\rho A)} \tag{5}$$

where T_H is the hovering thrust (N). It can be expressed as

$$T_H = \frac{\text{Thrust - to - weight Ratio} \times \text{Drone Weight}}{\text{No. of Rotor}} \tag{6}$$

The drag force acting on the drone during hover is unknown and therefore ignored. Thrust-to-weight ratio is included in Eq. (6). A general rule of thumb applied for quadrotor is that the thrust generated by the motors should be 1.5~2 times greater than the drone weight. This amount of thrust ensure enough power to lift the drone and still keeping sufficient power for user to control the drone (Hanford, Long and Horn 2005). Choosing 1.75 as the thrust-to-weight ratio, the hovering thrust required by each motor when the drone weight is 1.25kg and no. of rotor = 4 will be

$$T_H = 1.75(1.250 \times 9.81)/4 = 5.4N \tag{7}$$

Using Eq. (5), the theoretical rotational velocity of propeller

$$v_h = \sqrt{5.4/(2 \times 1.18415 \times \pi \times 0.115^2)} = 7.4 \,\text{m/s} \tag{8}$$

Note that this velocity will not be realistic enough as the propeller is subjected to viscous effects such as drag force in actual environment. However, it serves as an initial guess to determine the Reynolds number (Re) experienced by the propeller and therefore make it possible to begin this research with the airfoil selection for new propeller design. To calculate Re for the rotating propeller, engineers have typically chosen the cross section chord about 0.75R (Gamble and Arena 2009; Tracy 2011). Re is expressed as

$$\text{Re} = \rho V l / \mu \tag{9}$$

where l is the reference length (m), V is the

reference airspeed (m/s), ρ is the air density (kg/m^3) and μ is the air viscosity (=1.85508×10^{-5} Pa.s). At $V = v_h$ and chord length at 0.75R, $c =$ 0.022m, Re of the propeller is

$$\text{Re} = \frac{(1.18415)(7.4)(0.022)}{(1.85508 \times 10^{-5})} = 10403 \qquad (10)$$

For cruising case, the cruising thrust T_C is expressed as

$$T_C = DF = \tfrac{1}{2}\rho V^2 S C_D \qquad (11)$$

3. DESIGN METHODOLOGY

3.1 Numerical Model

SST K-Omega (SST k-ω) turbulence model is selected as the turbulence model for all 3 CFD models. It predicts the far field result based on K-Epsilon (k-ε) model and applied k-ω model to cater for the near wall formulation. An analysis done by Eleni, Athanasios, and Dionissios (2012) suggested SST k-ω as the most appropriate turbulence model for airfoil simulation among the three models (Spalart-Allmaras, Realizable k-ε and SST k-ω). The model equations can be found in their research paper.

3.2 Airfoil Model

Airfoil model was set up to study the flow characteristics and aerodynamic performances of various airfoils. As illustrated in Fig. 3, the test model consists of a curved inlet, two symmetry sides and one rectangular outlet.
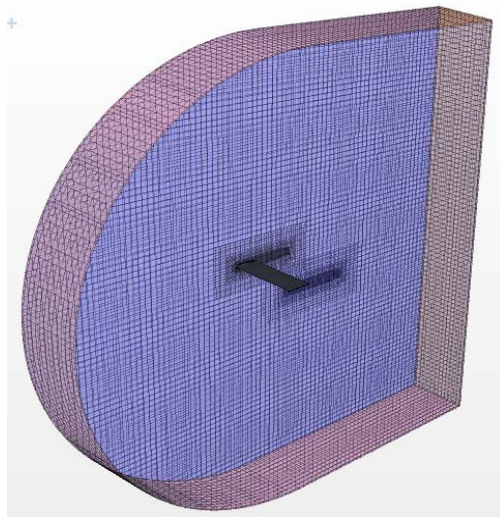

Fig. 3. 3D Airfoil Model.

An airfoil with a span of 15 inches is located at the centre of the region. Its chord length is 0.127 m, with a planform area of 0.048 m^2 (viewed from top). The dimension of the fluid domain is 2.54 m (h) × 2.54m (l) × 0.381m (w) with the radius of the curved inlet being 1.27 m, 10 times the chord length of the propeller to avoid any undesired effects of

boundary surface on the simulated result. As maximum thrust is required during hover condition to counteract the total drone weight with additional 400g payload, the airfoil would be selected by using the values based on hovering case. Inlet velocity was determined to be 1.2832 m/s given that Reynolds number of the airfoil is 10403. This model was run in steady state for 1000 iterations, with a convergence criteria of 3 orders of magnitude.

With this model, the lift and drag coefficients of all 6 airfoils (Benchmark, NACA 0012, NACA 4412, NACA 23012, Dillner 20-32C and Sokolov) were simulated at different AOA ($\phi = 2°$, 4°, 6°, 8°) to evaluate their aerodynamic performance listed in the design matrix (refer Table 1) with the most important parameter being lift-to-drag ratio. Airfoil which was rated the highest in the design matrix would be further investigated using the rotating propeller model and drone model to simulate the actual aerodynamic performance of the propeller where viscous effects are taken into account.

3.3 Rotating Propeller Model

As shown in Fig. 4, the computational domain of the rotating propeller model is 1.6 m (h) × 2 m (l) × 1 m (w), comprises of the outer fluid region and the inner rotating region. The inner region is a circular disc with 0.13 m radius and 0.07 m thickness which contains the wall surfaces of motor and propeller inside. To define the motion of the inner rotating regions, moving reference frame (rotating) was used. The rotational speed calculated ($\omega = v_h/r =$ 615 rpm) was inserted as the input for the rotation rate.
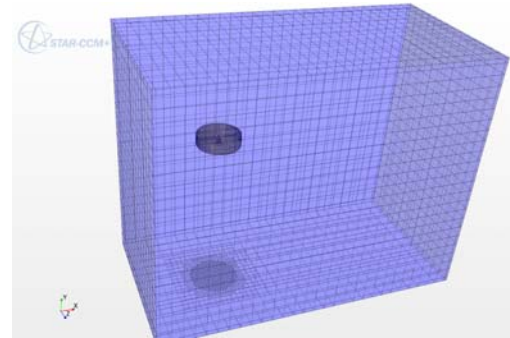

Fig. 4. Rotating Propeller Model.

Running for 1000 iterations with convergence criteria set at 0.001, this model was used to determine the thrust generated by a single propeller as it rotates at the motor shaft speed. The pre-determined rotational velocity was used to study the actual thrust generated. In case the velocity is not sufficient to produce the required thrust, the actual rotational velocity required could be estimated through trial and error via this model.

3.4 Drone Model

The dimension of the entire region of the drone model (Fig. 5) is 2.68 m (length) × 1.4 m (height) × 0.6 m (width). The drone was simulated in half due

to its symmetrical geometry. Two propellers that rotate in clockwise and anticlockwise direction respectively are assembled to the motors of the drone to further observe the aerodynamic performance of the propeller.
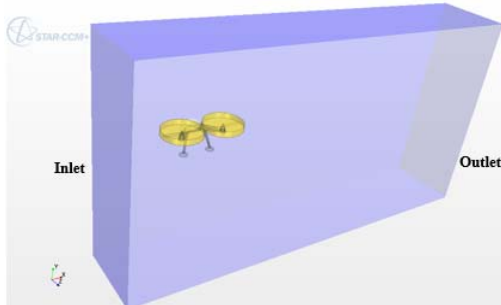

Fig. 5. Drone Model.

The drone height is 0.178 m, whereas maximum length and width are both 0.297 m. Rotating moving reference frames were applied to the two rotating regions with the rotation rate set at the actual rotational velocity required to produce 5.4 N thrust determined from previous propeller model. The simulation will be run in steady state for 2000 iterations to achieve a 2-order magnitude convergence criteria.

4. GRID INDEPENDENCE ANALYSIS

The 3 CFD models of this project were simulated in STAR-CCM+ v9.02. The meshes were generated by manually changing the base size of the model. To avoid using excessive amount of elements or cells in the model analysis which subsequently result in a waste of computational time, grid independent analysis were conducted to determine the appropriate mesh for the model.

4.1 Airfoil Model

The lift and drag coefficient generated by NACA 4412 airfoil with 0.127 m length at Re = 100 000 were obtained to determine the number of cells needed to achieve mesh independence. Inlet flow velocity was set at 12.3354 m/s.
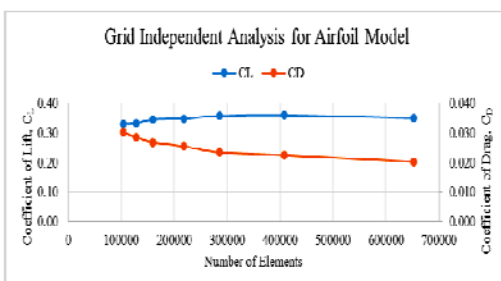
Fig. 6. Grid independence analysis for Airfoil model.

As depicted in Fig. 6, it was observed that the values of C_L became steadier as the number of elements continued to increase from 285000 but C_D

was still decreasing as the mesh was refined. This indicated that C_D was still mesh dependent. However, it was not advisable to further refine the mesh due to the increased computational time and cost. To select the suitable mesh to be used in the experiment, percentage error between each base size was compared in Table 1. From the table, it was observed that the percentage error between 0.030 m base size and 0.025 m base size was the lowest, at 0.63% for C_L and 4.03% for C_D. Hence, the base size of 0.03 m with 285527 cells was chosen for the airfoil model.

Table 1 Mesh independence results for airfoil model.

Base size (m)	No. of cells	C_D	% error	C_L	% error
0.050	103128	0.0303	-	0.330	-
0.045	128311	0.0285	5.75	0.333	0.74
0.040	159119	0.0268	6.10	0.344	3.5
0.035	218614	0.0254	5.05	0.348	0.97
0.030	285527	0.0234	8.13	0.357	2.70
0.025	407784	0.0224	4.03	0.359	0.63
0.020	652695	0.0202	9.94	0.350	2.66

4.2 Rotating Propeller Model

For rotating propeller model, the grid independence of the single motor and propeller configuration was conducted in hovering condition. The boundary condition for the inlet and outlet of the fluid region were therefore changed to symmetry plane which gave the wall shear stress as 0. From Fig. 7, it was discovered that the thrust generated became constant after the mesh elements increased to near 160 000. Hence, base size 0.07 m (168277 elements) was selected for propeller model simulation.
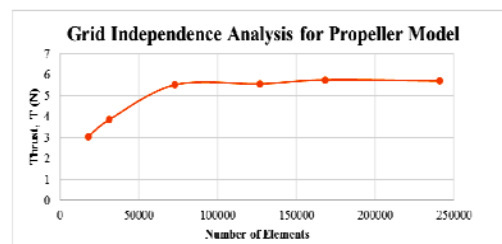
Fig. 7. Grid independence analysis for Rotating Propeller Model.

4.3 Drone Model

In the drone model, the C_L of the propeller in hover condition was used to check the grid independence of the model. The 3 simulated C_L values between 300 000 elements and 710 000 elements as shown in Fig. 8 were similar. The percentage error between these 3 C_Ls were found to be 1.27% and 0.68% respectively. There was not much difference between the model meshed at around 300 000 elements and 710 000 elements. Therefore, the model meshed with 298014 elements (base size = 0.06 m) was selected.
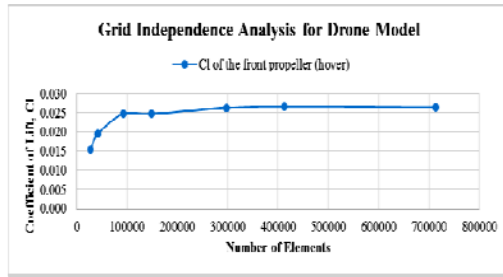
Fig. 8. Grid independence analysis for Drone model.

5. DATA VALIDATION

An experiment was conducted to validate the airfoil model by comparing the experimental mean velocity profiles around the airfoil with the simulated results. A symmetrical NACA 0020 airfoil specimen made from metal with smooth surface finish was used in the experiment. A schematic diagram of the experimental setup was shown in Fig. 9. It was tested in an open channel flow tank and the velocity profiles were measured using Ultrasonic Velocity Profiler (UVP) instrument as shown in Fig. 10. The experiment was conducted in water due to the working principle of the UVP instrument. Using UVP in air medium which gives weak sound echo would lead to poor results.
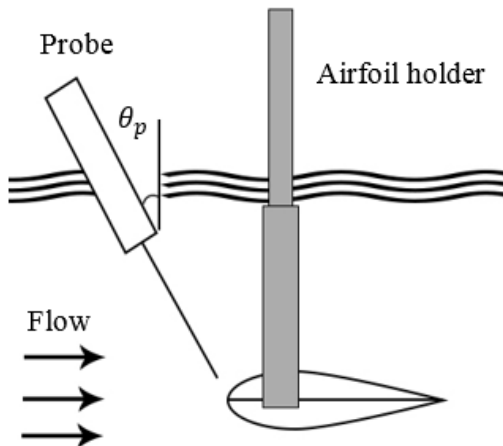

Fig. 9. Experimental setup of NACA 0020 in water.

The dimension of the tank is 0.7 m (h) × 1.8 m (l) × 0.7 m (w) with an inner measuring section of 0.5 m (h) × 0.8 m (l) × 0.5 m (w). The tank was filled with water to a depth of 0.3 m before experiment was carried out. Three submersible pumps installed at one end of the tank were used to circulate the water flow. The water were pumped into the connected PVC pipes which direct them to the sides of the frontal part of the tank. These two separated water flows were then directed to merge together and went through a honeycomb section to ensure uniform flow before entering the inner measuring section of the tank. As the water flew to the end of

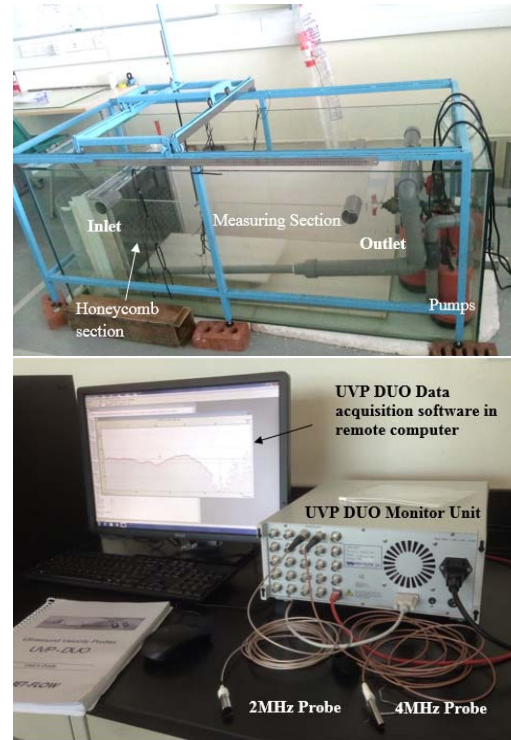the section, the submersible pumps pumped the water again and the water flow circulated.

Fig. 10. Open channel flow tank (top) and UVP instrument (bottom).

UVP measures the velocity profile of a liquid flow in a line along the ultrasonic beam axis of its transducer (probe). The ultrasonic transducer transmits ultrasonic pulses along the transducer axis where echoed ultrasound are reflected from the particles scattered in the flowing water back to the transducer. When the ultrasound wave is subjected to an incidence angle θ with respect to the flow normal (in degree), the liquid velocity can be obtained as

$$V = \frac{1}{\sin \theta} v \tag{12}$$

In this experiment, UVP measured the velocity profiles along the upper surface of the symmetrical airfoil with a 4 MHz transducer. The channel distance between each measurement point was 0.74 mm. With a fixed number of 165 channels, the profile measurement length was 112.1 mm. Active measurement length of the profile began at 5 mm from the head of the transducer. Transducer angle, θ_p as shown in Fig. 9 was 30 degree. At 128 repetitions with 4 cycles per pulse, the sampling time needed to obtain one single velocity profile is 640 ms. A total of 1000 samples (profiles) were taken to plot the average velocity profile at different x/c locations. It is difficult to obtain a uniform flow with consistent velocity in the experimental setup when the speed is too low. Hence, the flow speed was increased to reach Re = 45800 for the airfoil. The Re of the airfoil model was adjusted to the

experimental Re (45800) for comparison. Before immersing the airfoil into water, the AOA of the NACA 0020 airfoil relative to the flow direction was adjusted to zero degree. Average velocity profiles measured at two different location around the airfoil surface ($x/c=0$ and $x/c=0.2$) were analyzed and plotted in Fig. 11.
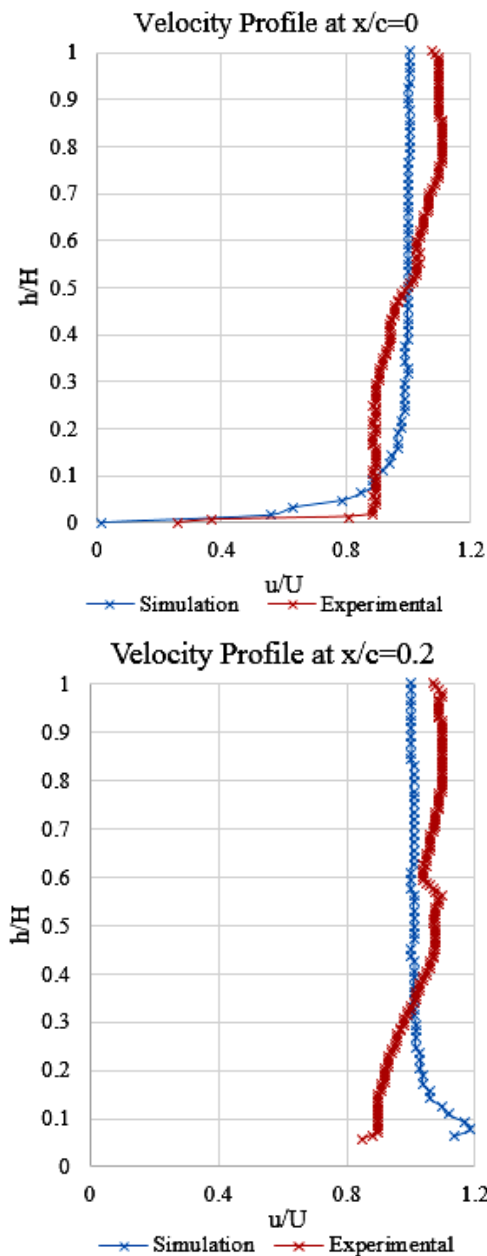

Fig. 11. Velocity profiles at *x/c*=0 (left) and *x/c*=0.2 (right) at Re = 45800.

The term x/c is the distance of location x measured from the airfoil leading edge with respect to its chord; h/H is the non-dimensional vertical distance measured from the airfoil chord line; and u/U is the dimensionless flow velocity.

At $x/c=0$, there was a sudden drop in the velocity magnitude near the airfoil surface. This indicated that a boundary layer formed on the airfoil surface

where viscous force slowed down the flow speed. At $x/c=0.2$, a hook-like curve was observed at the point nearest to the airfoil surface for both simulation and experimental results. However, the experimental flow velocity was lower than the average flow speed instead of being higher than the free stream flow as predicted in the simulation. This could be caused by the airfoil support rods which affected the water flow pattern and speed. From the two profiles, it could be seen that both experimental velocity profiles near the airfoil surface had similar trends as the simulated profiles. Therefore, it can be deduced that the results obtained from simulation model (airfoil model) were acceptable.

Apart from the experimental validation, the airfoil model was also compared with the readily available experimental data provided in NACA Report no. 613 (Pinkerton 1938) to prove that the 3D airfoil model could produce reasonable results. The airfoil dimension used in the simulation was kept the same as the experimental setup described in NACA Report no. 613, except for its span which was reduced by half due to symmetry. This could reduce the computational time since both side walls of the model were selected as symmetry plane condition.
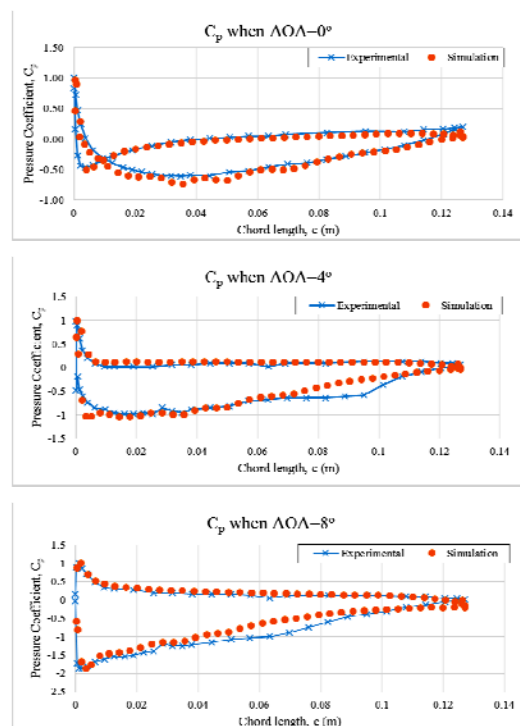

Fig. 12. Pressure coefficient of NACA 4412 when AOA = 0º, 4º and 8º.

The airfoil section used in the NACA report was NACA 4412, with a span of 0.762 m and a chord of 0.127 m. Pressure values had been measured at 17 AOAs ranging from -20º to 30º (Pinkerton 1938). Since the selected AOAs for airfoil simulation in this project were 0º, 2º, 4º, 6º and 8º respectively, 3 simulated results at AOA = 0º, 4º and 8º were picked to compare with the experimental pressure

coefficient. The experimental Reynolds number was 100 000. To maintain the Re at 100 000 in simulation, the inlet flow velocity of the airfoil model was set at 12.3354 m/s. Comparison between the simulated and experimental C_p were shown in Fig. 12.

As depicted in the figure, the simulation and experimental pressure coefficient distribution followed similar trends at different AOAs. Hence, this showed that the airfoil model was acceptable to be used for the airfoil simulation in this project, assuming that the results for Re at 10403 and 100 000 would be identical as they both were in the range of low Reynolds number (< 200 000).

5. RESULTS AND DISCUSSIONS

Airfoil model was used to study the lift and drag characteristics of respective airfoils at different AOAs whereas the amount of thrust generated by the propeller was determined in rotating propeller method, and lastly the aerodynamic performance of the drone using the selected propellers was evaluated in the drone model with different propeller configurations. The results for each simulation were shown in this chapter.

5.1 Effect of Angle of Attack

With each increment of 2 degrees in the AOA, the lift coefficient of the airfoils increases linearly as shown in Fig. 13. This relationship between AOA and lift coefficient is valid as long as the stalling angles of the airfoils have not been reached. Note that the stalling angle changes at different Re. For instance, the stalling angle of NACA 0012 at Re = 3×10^6 is 16º (Eleni, Athanasios, and Dionissios 2012) but reduces to 14º when Re = 1×10^5 (Corrêa, Paula Sales, Alves Rade, and Souza 2014). From the constant increment of lift coefficient, it can be deduced that the stalling angles for all the airfoils at Re = 10403 are greater than 8º as there is no sudden loss of lift observed at high AOA.
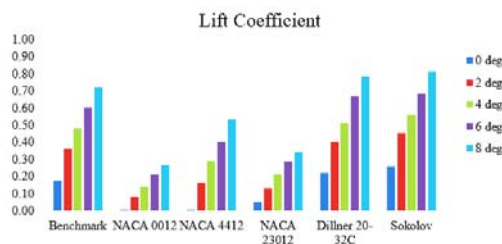

Fig. 13. Lift coefficient of various airfoils at different AOAs at Re=10403.

Among the 5 proposed airfoils, Dillner 20-32C and Sokolov are the only two airfoils that produce more lift than the benchmark airfoil at all AOAs. The airfoil that exhibits the highest lift is Sokolov. Overall, the symmetrical NACA 0012 has the lowest C_L as expected. Surprisingly, the cambered NACA 4412 airfoil gives the lowest C_L (0.0005) among the 6 airfoils when the AOA is 0º. This

indicates that the zero lift angle α_{ZL} of NACA 4412 is near 0º. As AOA increases, its lift coefficient rises immediately and beats NACA 0012. It is discovered that the lifting capability of an airfoil at higher AOAs will increase substantially with the introduction of camber.

Fig. 14 shows that the drag force acting on the airfoil also increases with higher AOA but at a slower pace. The increasing rate of C_D becomes quicker with the increment in AOA. At AOA = 8º, the induced drag of all airfoils are more than two fold than at AOA = 0º. For instance, the C_D of benchmark airfoil increases from 0.0492 to 0.1059. Airfoil geometry which induces the greatest C_D is Dillner 20-32C (C_D = 0.1270 at 8º).
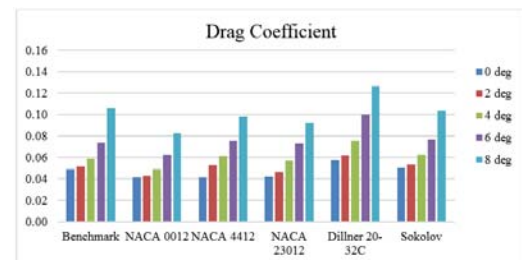

Fig. 14. Drag coefficient of various airfoils at different AOAs at Re=10403.

The airfoil lift-to-drag ratios at respective AOAs are shown in Fig. 15. Optimal aerodynamic performance is only achievable by making a compromise between the lift and drag. The importance of keeping lift-to-drag ratio as a design parameter is easier to understand by observing the benchmark and Dillner 20-32C. As discussed earlier, Dillner 20-32C has higher C_L compare to benchmark, but at the same time, it generates a higher C_D as well. If the airfoil selection is solely based on the lifting capability of an airfoil, Dillner 20-32C is definitely better. However, looking from the aspect of lift-to-drag ratio, Dillner 20-32C performs poorer than the benchmark airfoil when AOA increases which indicates that latter gives better aerodynamic performance.
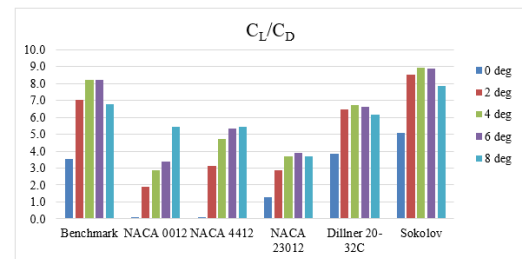

Fig. 15. Lift-to-drag ratio of various airfoils at different AOAs.

It is observed that the decline in lift-to-drag ratio between the range of 4º and 8º happens to all the cambered airfoils except NACA 4412. This could be due to the flow separation of air near the airfoil

surface. As the AOA increases, the airfoil is tilted upwards and it can be expected that the flow will separate earlier at 8º rather than 4º or 6º. Therefore the lift produced will be smaller and the drag will increase. This results in lower lift-to-drag ratio. As depicted in Fig. 15, Sokolov airfoil outperforms all the other airfoils at every AOA in terms of lift-to-drag ratio. The peak lift-to-drag ratio of Sokolov occurs at 4º, with a value of 8.948, followed by 8.868 at 6º. It is the only airfoil among the five which surpass the benchmark airfoil. Therefore, Sokolov has the highest rating in this criterion.

5.2 Airfoil Selection (Design Matrix)

A design matrix as shown in Table 1 is proposed to select the most suitable airfoil. The total points of each airfoil is obtained by multiplying the rated values with the weightage and sum up. The relative total is then calculated by dividing the total points of the airfoil with the maximum total points (Total weightage × 5).

Table 1 Completed Design Matrix for Airfoils (5 = good, 3 = average, 1 = bad)

Parameters	Weight-age	Benchmark	NACA 0012	NACA 4412	NACA 23012	Dillner 20-32C	Sokolov
Camber	10	5	1	3	1	5	3
Maximum thickness	10	5	1	1	1	3	5
C_L	20	3	1	3	1	3	5
C_D	15	3	5	3	3	1	3
C_L/C_D	25	5	1	3	1	3	5
Ease of Manufacture	10	3	5	3	3	3	3
Total	100	360	190	250	140	300	380
Relative total		0.72	0.38	0.50	0.28	0.60	0.76

Among the 6 airfoils, Sokolov is rated the highest at 0.76. Hence, Sokolov airfoil is selected for the development of new propeller design in the later stage. Using XFoil, QMIL, MATLAB and Solidworks, a solid propeller is generated based on the Sokolov airfoil geometry.

5.3 Thrust generation of Original and Modified Propeller

The benchmark propeller as shown in Fig. 16 is first simulated in rotating propeller model with 615 rpm inserted as the input rotation rate of the moving reference frame.

It is found that the theoretical rotational velocity is insufficient to provide the thrust. This is expected as the theoretical calculation has not taken the viscous drag generated by the propeller into account. Through the method of trial and error, the required 5.4 N thrust is found to be generated by the benchmark propeller when the rotation rate increases to 7750 rpm. This is then followed by the testing of Sokolov propeller (Fig. 17) at both rpms.

The thrust results are tabulated in Table 2.

Fig. 16. Top and Side view of the benchmark Propeller.

Fig. 17. Top and Side view of the new Sokolov propeller.

Table 2 Thrust generated by Benchmark and Sokolov Propeller

Propeller	Thrust at 615 rpm (N)	Thrust at 7750 rpm (N)
Benchmark	0.032	5.39
Sokolov	0.037	6.15

5.4 Thrust and drag in Hovering and Cruising Conditions

By setting the rotation rate of both rotors to be zero, the drag coefficient of WL-V303 Seeker quadrotor can be simulated in drone model to determine the forward thrust required. At a cruising velocity of 5 m/s, the C_D of the drone installed with a rectangular payload is found to be 1.09. Provided the total frontal area of the drone is 0.192 m², using Eq. (11), the required forward thrust to counteract the drag will be 0.31 N. Since the drone is simulated in half, there are only two propellers in the model. The total value of T_H and T_C in Table 3 are calculated by adding up the thrust generated by these two propellers.

For a hovering drone, it is expected that each rotor will generate the same amount of thrust. Based on the results shown in Table 2, it can be approximated the total hovering thrust generated by two propellers will be double the value, which is 10.78 N for two benchmark propellers and 12.30 N for two Sokolov propellers. However, it is noticed that the hovering thrust generated by the two propellers is lower than the expected value as shown in Table 3.

Table 3 Thrust and drag of drone with different propellers

Configuration	Hovering condition		Cruising condition	
	T_H (N)	D_V (N)	Tc (N)	C_D
Benchmark	9.58	0.78	0.015	-0.044
Sokolov	11.96	1.46	0.036	0.84

A quadrotor can be controlled to fly in different directions by varying each rotor speed. To move forward, the rotors on the front will be spinning slower, generating less thrust and the rotors behind will rotate faster to make up for the thrust lost such that the total thrust generated maintains. Due to the differential thrust, the front part of the drone will incline downward from the horizontal plane by an angle. This angle and the changes in rotor speed have not been taken into account in the simulation. Apart from that, the two propellers which rotate in different direction have their propeller tips close to one another. Hence, the air flow between these two propellers might interfere with each other and reduces the amount of lift generated.

5.5 Effect of Propeller Configuration on Thrust and Drag

The effects of propellers configuration on the drone thrust and C_D were studied by switching the position of the two counter rotating propellers with each other. There are two configurations: Front-CW and Front-ACW, as shown in Fig. 18.
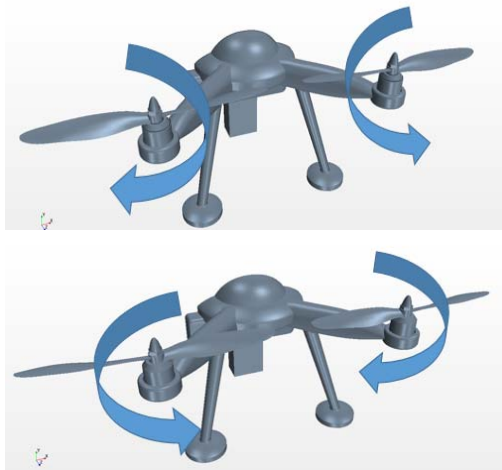
Fig. 18. Propeller Configurations; (top) Benchmark (Front-CW), (bottom) Benchmark (Front-ACW).

The current WL-V303 Seeker Quadrotor has Benchmark (Front-CW) propeller configuration. The simulation results for both configurations at 7750 rpm using benchmark and Sokolov propellers are shown in Table 4.

The drag force experienced by the quadrotor in hover is denoted as vertical drag D_V whereas in cruising state, the streamwise drag is denoted as D_S. The highest T_H and Tc (13.74 N and 0.038 N) are

recorded with Sokolov (Front-ACW) configuration in both hovering and cruising conditions. However, the highest lift-to-drag ratios are given by the benchmark (Front-ACW) configuration, which are 17.14 and 0.33 respectively. Despite generating lower thrust, the benchmark propellers in both configurations generate less drag. This strength balances their weakness in lift force generation and keep their lift-to-drag ratio higher than the Sokolov propellers.

Table 4 Thrust and drag of drone in different propeller configurations

Configuration	Hovering Condition			Cruising Condition		
	T_H (N)	D_V (N)	$\dfrac{T_H}{D_V}$	Tc (N)	D_S (N)	$\dfrac{T_C}{D_S}$
Benchmark (Front–CW)	9.58	0.78	12.28	0.015	-0.044	-
Benchmark (Front–ACW)	10.97	0.64	17.14	0.026	0.079	0.33
Sokolov (Front–CW)	11.96	1.46	8.19	0.036	0.46	0.08
Sokolov (Front–ACW)	13.74	0.94	14.62	0.038	-0.205	-

5.5.1 Hovering Condition

It is discovered that the Front-ACW configuration gives higher thrust and lower drag. This occurs for both propeller types (Benchmark and Sokolov). The vertical drag of the drone in Front-ACW configuration is reduced when compared to the Front-CW configuration (refer Table 4). The difference is probably due to the flow characteristics around the drone as shown in Fig. 19.
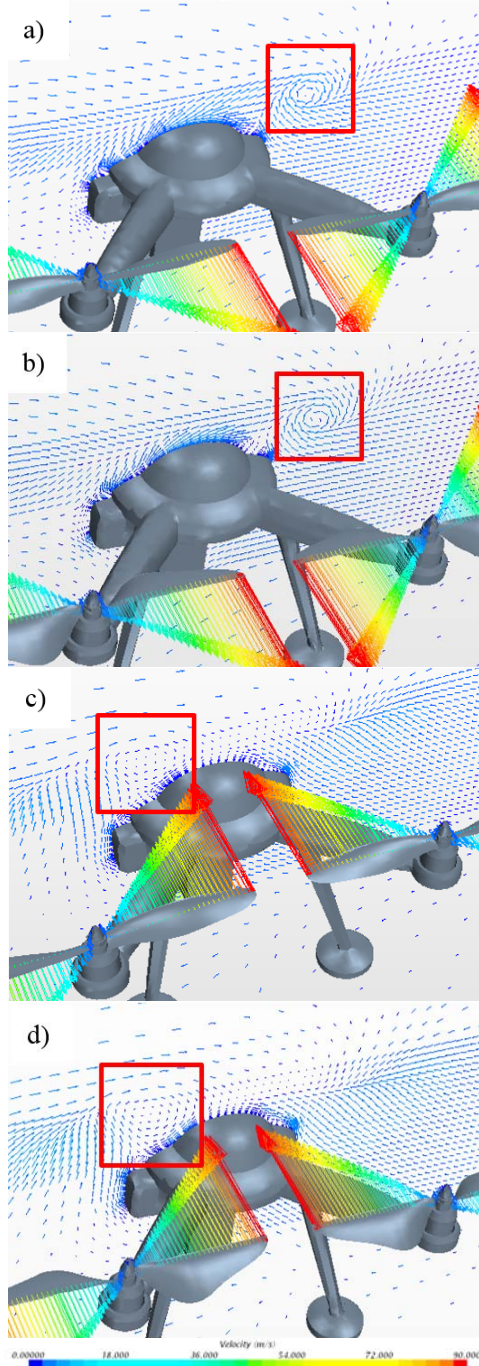
It is observed that the flow patterns near the drone surface for Front-CW and Front-ACW configurations are different. For Front-CW configuration, visible vortical flow forms behind the drone. The larger vortex area observed infers that the drone experiences a stronger circulation (Dol 2013). This can be seen by the velocity vectors in the vortical flow which are in light blue colour, denoting higher velocity. Although stronger circulation generally means higher lift, note that the direction of vortex leaving the drone is moving in CW direction, so the circulation around the drone to resist the vortex will be in ACW direction. ACW circulation is considered positive. As the circulation is positive, Eq. (3) will give a negative lift. This explains why the drone will experience higher drag.

As for the Front-ACW configuration, vortical flow forms above the head of the drone in Fig. 19 (c) and (d) is less visible, indicates that the vortex strength is weaker, contributing to smaller negative lift (Dol 2013). Therefore, Front-ACW configuration will be able to reduce the drag experienced by the quadrotor. By changing the configuration of benchmark (Front-CW) to benchmark (Front-ACW), the hovering performance in terms of lift-to-drag ratio increases by 39.58%.

5.5.2 Cruising Condition

The forward thrust T_C obtained from the simulation

is very minimal compare to the hovering thrust T_H. This is because the propellers are rotating with respect to the vertical axis, therefore only minimal thrust can be obtained from the drone that is in perfectly horizontal position. Negative values of streamwise drag as shown in the benchmark (Front-CW) and Sokolov (Front-ACW) configurations in Table 4 indicate that the drone does not experience drag force in streamwise direction at these two configurations.

In cruising state, the flow characteristic around the drone have changed. As depicted in Fig. 20, for benchmark (Front-CW) configuration, vortical flow can still be observed behind the drone. The vortex area has grown larger with higher velocity as the incoming flow now has a relative velocity of 5 m/s.

Fig. 19. Vortical flow (in red square region) spotted around drone with (a) Benchmark (Front-CW); (b) Sokolov (Front-CW); (c) Benchmark (Front-ACW) and (d) Sokolov (Front-ACW) propeller configuration in hover state.
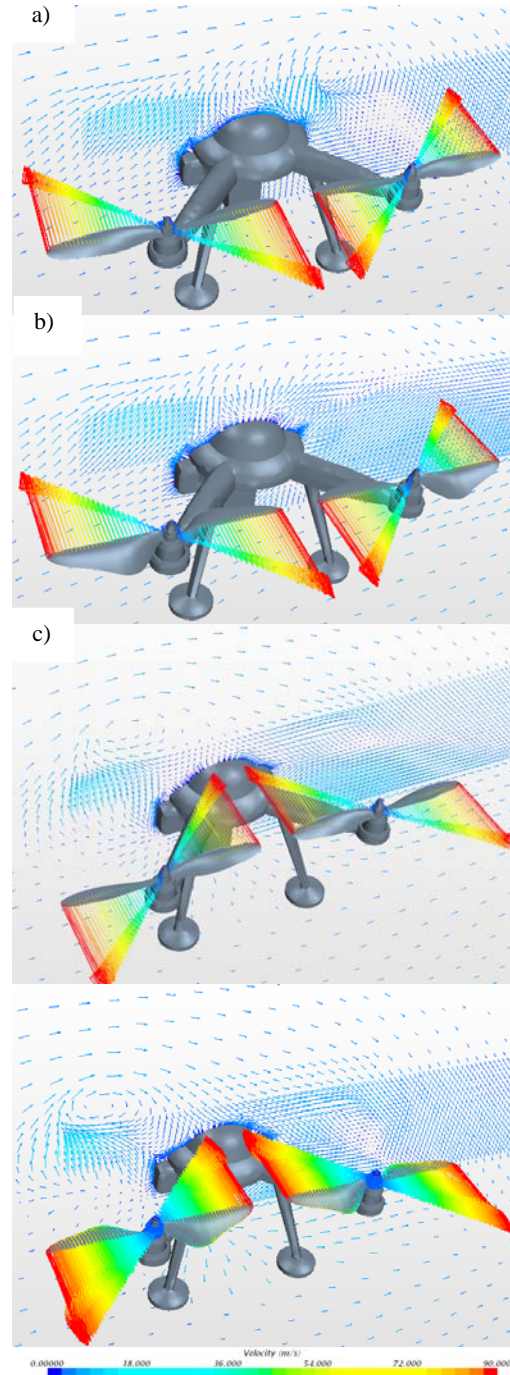
Fig. 20. Flow around drone with (a) Front-CW (Benchmark); (b) Front-CW (Sokolov); (c) Front-ACW (Benchmark) and (d) Front-ACW (Sokolov) propeller configuration in cruise.

However, this phenomenon is absent for Sokolov (Front-CW) configuration. This is possibly due to

the larger surface area and curvy shape of the Sokolov propeller blade which directed the air flow downwards when it flows through the propeller blade. Hence, velocity increases at the lower region behind the drone. As for the Front-ACW configuration for both type of propellers, the strength of the circulation forming above the frontal part of the drone have grown stronger.

Looking at the values of forward thrust and streamwise drag in Table 4, it is noticed that the Sokolov propeller induced much higher drag to the drone than the benchmark propeller although the forward thrust is slightly higher. Hence, further research on the Sokolov propeller design is necessary to reduce the induced drag.

5. CONCLUSION

The aerodynamic performance of a quadrotor propeller had been investigated extensively from the stage of airfoil selection to the final assembly of the drone via CFD method. Among the 5 airfoils evaluated, Sokolov airfoil with the highest lift-to-drag ratio was selected to improve the current propeller. The amount of thrust generated by the new Sokolov propeller was compared with the benchmark propeller in the rotating propeller model. It was observed that the Sokolov propeller generated higher thrust than the benchmark propeller at 7750 rpm. However, the drone had a higher lift-to-drag ratio with the use of benchmark propeller. Sokolov propellers were outperformed by benchmark propellers in the drone model due to higher induced drag. Nonetheless, it was revealed that the aerodynamic performance of the drone could be improved by switching the current rotor configuration to rotate in the opposite direction. Further studies can be conducted by including the drone's pitching angle into the simulation and conduct experiments to validate the propeller and drone models.

ACKNOWLEDGEMENTS

REFERENCES

Corrêa, A., F. Medina, T. de Paula Sales, D. Alves Rade and F. José de Souza (2014). Study of the Flow over an Oscillating Naca0012 Airfoil.

Dol, S. S. (2013). Weakened Vortex Shedding from a Rotating Cylinder. *International Journal of Mechanical, Aerospace, Industrial, Mechatronic and Manufacturing Engineering* 7(10), 1679-1686.

Dol, S. S., G. A. Kopp and R. J. Martinuzzi (2008). The suppression of periodic vortex shedding from a rotating circular cylinder. *Journal of Wind Engineering and Industrial Aerodynamics* 96(6), 1164-1184.

Eleni, D. C., I. A. Tsavalos and P. D. Margaris (2012). Evaluation of the Turbulence Models for the Simulation of the Flow over a National Advisory Committee for Aeronautics (Naca) 0012 Airfoil. *Journal of Mechanical Engineering Research* 4(3), 100-111.

Gamble, D. E. and A. Arena (2009). Automated Dynamic Propeller Testing at Low Reynolds Numbers. Oklahoma State University.

Gudmundsson, S. (2014). Chapter 14 - the Anatomy of the Propeller. In *General Aviation Aircraft Design*, ed. Snorri Gudmundsson 581-659.

Hanford, S. D., Lyle N. L. and J. F. Horn (2005). A Small Semi-Autonomous Rotary-Wing Unmanned Air Vehicle (UAV). *AIAA2005-7077*.

Hardi, P. and R. Schlichenmaier (2005). *Introduction to Hydrodynamics. Freiburg.*

Pinkerton, R. M (1938). The variation with Reynolds number of pressure distribution over an airfoil section 613.

Tracy, I. P. (2011). *Propeller Design and Analysis for a Small, Autonomous UAV*. Massachusetts Institute of Technology.

Yahya, S. M. (2010). *Turbines Compressors and Fans*: Tata McGraw-Hill Education

Yeong, S. P., L. M. King and S. S. Dol (2015). A Review on Marine Search and Rescue Operations Using Unmanned Aerial Vehicles. *International Journal of Mechanical, Aerospace, Industrial, Mechatronic and Manufacturing Engineering* 9(2), 390-393.

Yogianandh, N., R. Stopforth and G. Bright (2011). Quad-Rotor Unmanned Aerial Vehicle Helicopter Modelling and Control. *Int J Adv Robotic Sy* 8(4), 139-149.